PHYSICAL REVIEW MATERIALS **5**, 044407 (2021)

Competing magnetic states in multiferroic $BaYFeO_4$: A high magnetic field study

D. P. Kozlenko,[1,*] N. T. Dang,[2,3,*] R. P. Madhogaria,[4] L. T. P. Thao,[5,6,*] S. E. Kichanov,[1] N. Tran,[2,3] D. T. Khan,[6]
N. Truong-Tho,[5] T. L. Phan,[7] B. W. Lee,[7] B. N. Savenko,[1] A. V. Rutkauskas,[1] L. H. Khiem,[8,9] H. B. Nguyen,[10]
T. A. Tran,[11] T. Kmječ,[12] J. Kohout,[12] V. Chlan,[12,*] and M. H. Phan[4,*]
[1]*Frank Laboratory of Neutron Physics, Joint Institute for Nuclear Research, 141980 Dubna, Russia*
[2]*Institute of Research and Development, Duy Tan University, 550000 Danang, Vietnam*
[3]*Faculty of Natural Sciences, Duy Tan University, 550000 Danang, Vietnam*
[4]*Department of Physics, University of South Florida, Tampa, Florida 33620, USA*
[5]*Faculty of Electronics, Electrical Engineering and Material Technology, University of Sciences, Hue University, 530000 Hue, Vietnam*
[6]*University of Science and Education, The University of Danang, 550000 Danang, Vietnam*
[7]*Department of Physics and Oxide Research Center, Hankuk University of Foreign Studies, Yongin 449-791, South Korea*
[8]*Institute of Physics, Vietnam Academy of Science and Technology, 100000 Hanoi, Vietnam*
[9]*Graduate University of Science and Technology, Vietnam Academy of Science and Technology, 100000 Hanoi, Vietnam*
[10]*Institute for Missile, Institute of Military Science and Technology, 100000 Hanoi, Vietnam*
[11]*Ho Chi Minh City University of Technology and Education, 700000 Ho Chi Minh, Vietnam*
[12]*Faculty of Mathematics and Physics, Charles University, V Holešovičkách 2, Prague 18000, Czech Republic*

(Received 24 December 2020; revised 19 March 2021; accepted 30 March 2021; published 19 April 2021;
corrected 17 August 2023)

Spin-driven ferroelectricity phenomena have drawn great interest in the scientific community due to potential application in spintronics and their complex physical mechanisms. A noticeable example of this is multiferroic $BaYFeO_4$ that exhibits an unconventional magnetoelectric (ME) coupling due to the uncorrelated behavior of the ferroelectric and cycloidal states under an applied magnetic field. To shed more light on this spin-driven ME effect, a high-quality sample of $BaYFeO_4$ was synthesized by a standard solid-state reaction method, and its high-field (up to 9 T) magnetic properties have been systematically investigated by means of magnetometry, magnetocaloric effect, and Mössbauer measurements over a wide temperature range (5–400 K). In addition, its crystal and magnetic structures have been studied using x-ray and neutron powder diffraction. Results obtained indicate that Fe spins form a long-range spin density wave (SDW) antiferromagnetic (AFM) order at $T_{N1} \sim 50$ K, which transforms into the cycloidal AFM order at $T_{N2} \sim 35$ K. A spin-glass-like state emerges below $T^* \sim 17$ K, and coexists with the long-range cycloidal AFM one in this temperature range. Magnetocaloric and Mössbauer measurements consistently confirm the robustness of both the long-range SDW and cycloidal AFM orders under applied magnetic fields up to 6 T, whereas the spin-glass state is converted into the ferromagnetic (FM) state when the applied magnetic field exceeds 1 T. These findings pinpoint the fact that the magnetic field evolution of spin correlations from the AFM to FM character in the spin-glass state is responsible for the magnetic field dependence of ferroelectricity in $BaYFeO_4$.

DOI: 10.1103/PhysRevMaterials.5.044407

I. INTRODUCTION

Multiferroic materials, where ferroelectricity is induced by magnetic order, are of great interest because of their potential applications in electronic devices and their intriguing physical phenomena, such as the magnetoelectric (ME) effect, the generation of electromagnons, etc. [1–6]. The strong ME coupling makes them promising for use in multifunctional devices with electric-field-tunable magnetism and magnetic-field-controlled ferroelectricity [1–6]. Usually, the ME effect has been discovered in materials with peculiar long-range magnetic structures, such as noncollinear incommensurate cycloidal antiferromagnetic (AFM) $RMnO_3$ (R = Tb, Dy, Ho, Er) [1,4,7,8], $MnWO_4$ [9] and $CoCr_2O_4$ [10], E-type collinear commensurate AFM $RMnO_3$ (R = Tm) [11], Ca_3CoMnO_6 [12], and modulated incommensurate and commensurate AFM RMn_2O_5 (R: rare-earth elements) [13,14]. The ferroelectricity induced by a noncollinear magnetic structure is generally explained by the spin-current model based on antisymmetric Dzyaloshinskii-Moriya interactions, in which the electric polarization is induced by the vector spin chirality $k = S_i \times S_j$, where S_i and S_j are adjacent i and j spins, respectively [15,16]. In case of the collinear E-type magnetic phase, the applicable mechanism is the symmetric exchange-striction one, providing an electrical polarization proportional to the scalar product of adjacent spins $P_e \sim S_i.S_j$ [4,17]. On the other hand, the ME effect has been discovered in magnetically disordered systems, such as spin glasses $Ni_{1-x}Mn_xTiO_3$ [18], $La_3Ni_2NbO_9$ [19], Fe_2TiO_5 [20], $Rb_2Cu_2Mo_3O_{12}$ [21] or some spin liquids like $YBaCo_3FeO_7$ [22]. Besides, the vector spin chirality, other

---

[*] Corresponding authors: denk@nf.jinr.ru; dangngoctoan1@duytan.edu.vn; ltpthao@ued.udn.vn; chlan@mbox.troja.mff.cuni.cz; phanm@usf.edu

2475-9953/2021/5(4)/044407(14)

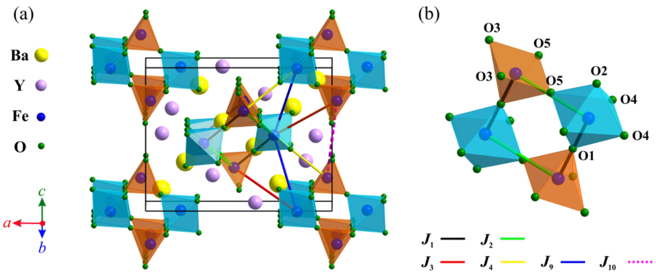

FIG. 1. (a) The crystal structure of $BaYFeO_4$. The paths of the intra- (J_1, J_2) and interchain (J_3, J_4, J_9, J_{10}) interactions are illustrated. (b) Corner-shared octahedra FeO_6 and square pyramids FeO_5 forming Fe_4O_{18} rings. Five crystallographic positions for oxygen atom are denoted.

multispin variables like the toroidal moment $t = \sum_i r_i \times S_i$, where r_i denotes the location of spin S_i, and the scalar spin chirality $\chi = S_i[S_j \times S_k]$ have also been proposed to contribute to the ferroelectricity and ME coupling in the absence of a long-range magnetic order [18,23,24]. For instance, it has been shown that the long-range vector spin chirality order in $Rb_2Cu_2Mo_3O_{12}$ [21], or the toroidal ordering in $Ni_{1-x}Mn_xTiO_3$ [18,25], or the scalar spin chirality coupling in the spin liquid $YBaCo_3FeO_7$ [22] can induce the ferroelectricity and ME coupling.

Recently, $BaYFeO_4$ has been reported to exhibit the spin-driven ferroelectricity along with unusual magnetic properties, but the magnetic field-induced ME mechanism remains a fully unanswered question [26–29]. In the orthorhombic *Pnma* crystal structure of $BaYFeO_4$ [Fig. 1(a)], there are two crystallographic sites for transition-metal ions at centers of alternating corner-sharing octahedra $Fe^{3+}O_6$ and square pyramids $Fe^{3+}O_5$, forming Fe_4O_{18} tetramers [Fig. 1(b)] [27,28]. The tetramers via edge sharing form folded-ladder chains running along the *b* axis (Fig. 1). The intrachain magnetic interaction between iron ions is mediated mostly through dominant strong AFM Fe-O-Fe superexchange interactions J_1 and J_2 (see Fig. 1), causing the collinear AFM alignment between nearest-neighbor Fe^{3+} spins inside each chain [26–28]. The interchain magnetic interaction is determined by the competition between the weak Fe-O-O-Fe super-superexchange magnetic interactions J_3, J_4, J_9, and J_{10} labeled as in Ref. [26]. The comparable strength of the interchain magnetic interactions combined with their peculiar geometrical arrangement gives rise to magnetic frustration [26], and the formation of competing magnetic states. [27,28,30]. $BaYFeO_4$ has been reported to exhibit three magnetic transitions at $T_{N1} \sim 48$ K, $T_{N2} \sim 33$ K, and $T^* \sim 17$ K [27,28,30]. Using neutron diffraction measurements, Thomson *et al.* [27] proposed that the highest magnetic transition temperature corresponds to the onset of a long-range commensurate spin density wave (SDW) AFM order with the propagation vector $k = (0, 0, \frac{1}{3})$ and Fe^{3+} spins pointing along the axis *b*, which then transforms at T_{N2} into an incommensurate cycloidal one with $k = (0, 0, 0.35)$ and the moments rotating within the *bc* plane. A spin-cluster glass state was observed below $T^* \sim 17$ K [31]. Lately, Cong *et al.* revealed the occurrence of ferroelectricity with a strong ME coupling effect around T_{N2}, relating this to the cycloidal magnetic order [29]. Notably, an additional broad dielectric permittivity peak was also observed at $T \sim 22$ K, in the vicinity of T^*, suggesting a strong impact of the spin-glass state on the ME response of $BaYFeO_4$ [29]. However, its origin remains has remained unexplored. It should be noticed that systems with the strong ME effect usually show a closely correlated behavior between the changes of the spin arrangement and the polarization. While the ferroelectric state in $BaYFeO_4$ was observed to be significantly suppressed by the application of external magnetic fields *H* above 1 T [29], recent magnetic susceptibility and specific heat measurements have revealed the robustness of both the long-range SDW and cycloidal AFM states under *H* up to 9 T [30]. Therefore, the origin of the ME effect in $BaYFeO_4$ is not fully understood, which thus warrants a more thorough high magnetic field study.

To provide deeper insights into the aforementioned ME effect, we have performed a systematic high-magnetic-field study of $BaYFeO_4$ up to 9 T by means of magnetometry, magnetocaloric effect (MCE), and Mössbauer measurements. In addition, temperature-dependent x-ray and neutron powder diffraction measurements were performed. Our results have shown that the spin-glass-like state plays an important role in the magnetic field evolution of ME in this material system.

II. EXPERIMENTAL DETAILS

The $BaYFeO_4$ sample was prepared from stoichiometric mixtures of $BaCO_3$, Y_2O_3, and Fe_2O_3 (purchased from Sigma Aldrich, purities $\geqslant 99.9\%$) by the solid-state reaction method. All precursors were dried before weighing. The mixtures were ground, pressed into a pellet, and annealed in air on an Al_2O_3 crucible at 900 °C for 12 h. After the first annealing, the sample was sintered five times at 1250 °C for 24 h (with grinding and pellet pressing after each step).

The crystal structure of the sample was characterized by an x-ray diffractometer D8Advance Eco (Bruker) equipped with a Cu-$K\alpha$ radiation source ($\lambda = 1.54056$ Å). X-ray diffraction (XRD) data was recorded in the angle range $2\theta = 20$–70° with the scanning step and scanning speed fixed at 0.01 ° and 1 °/min, respectively. The neutron powder-diffraction (NPD) measurements in the temperature range of $T = 15$–300 K were performed with the DN-12 diffractometer (IBR-2 pulsed reactor, JINR, Russia) [32]. NPD patterns were collected at scattering angles of $2\theta = 45.5^\circ$ and 90° with resolutions of $\Delta d/d = 0.022$ and 0.015, respectively. The typical data collection time for each temperature was 4 h. The experimental data were analyzed by the Rietveld method using the FULLPROF program [33].

Magnetic measurements were performed using a Quantum Design Physical Property Measurement System (PPMS) with a vibrating sample magnetometer. Magnetization versus applied magnetic field (*M* vs *H*) curves were measured at the *H* range of 0−9 T for temperatures ranging from 2 to 300 K. Using the AC/DC magnetometry system option of the PPMS, ac susceptibility measurements were performed with frequencies ranging from 111 to 444 Hz at an *ac* driving field of 5 Oe while warming up from 3 K. Temperature dependence of remanent magnetization was measured by a superconducting quantum interference device magnetometer MPMS-7

(Quantum Design). The sample was first cooled down to 2 K and then it was magnetized by field 7 T, which was lowered to 0. Finally, residual magnetization was measured during increase of the temperature up to 70 K using sweep regime 1 K/min.

For Mössbauer spectroscopy experiments, the pressed tablets of a diameter of 13 mm were prepared from ~15 mg of powdered sample with addition of ~50 mg of tableting wax. The ^{57}Fe Mössbauer spectra were collected in transmission geometry with a conventional spectrometer (WissEl GmbH., Germany) working in the constant-acceleration mode, equipped with a ^{57}Co(Rh) source. Calibration of the velocity scale was performed by an α-Fe foil at room temperature; the values of the isomer shift are given relative to the center of its Mössbauer spectrum. The temperature-dependent spectra were acquired in a Janis bath cryostat from 4.2 K to room temperature. The in-field spectra were obtained at required temperatures in external magnetic fields of 2–6 T oriented perpendicularly to the direction of the γ beam. The spectra were evaluated using the CONFIT [34] and MOSSWINN [35] fitting software.

III. RESULTS AND DISCUSSION

A. x-ray and neutron diffraction

The crystalline properties of the synthesized sample at room temperature were checked using a combination of the XRD and NPD methods. The results are shown in Fig. 2. The Rietveld refinement of the XRD and NPD data using the previously reported structural model of $BaYFeO_4$ has revealed that the sample is a single phase and has the *Pnma* orthorhombic crystal structure with lattice parameters $a = 13.1412(2)$ Å, $b = 5.6938(1)$ Å, and $c = 10.2451(2)$ Å [27,28]. It is noteworthy that in contrast to XRD, NPD allows accurate determination of oxygen parameters even in the presence of heavier cations due to the irregular variation of neutron scattering length with atomic number. As can be seen in Fig. 2(b), a good agreement between the NPD data and structural model was achieved with acceptable R factors, $R_p = 4.17\%$ and $R_B = 7.80\%$. The obtained values of the structural parameters and relevant interatomic Fe-O distances are listed in Table I. The obtained results are consistent with those previously reported in Refs. [27,28]. Moreover, the average crystallite size and microstrain can be estimated from the XRD data using the Williamson-Hall method based on the $2\theta_{hkl}$ position dependence of peak broadening value β_{hkl} after subtracting the instrumental broadening contribution [36,37]. According to the Williamson-Hall method, the line broadening β_{hkl} of a diffraction reflection ($h\ k\ l$) is the sum of the broadening $\beta_D = \frac{K\lambda}{D\cos(\theta_{hkl})}$ originating from the small crystallite size and the strain-induced broadening $\beta_\varepsilon = 4\varepsilon\tan(\theta_{hkl})$ [36,37]. Here, K is the shape factor, λ is the x-ray wavelength, D is the effective crystallite size normal to the reflecting planes, and ε is the root mean square value of the microstrain [36,37]. Furthermore, the microstrain and the crystallite size can be estimated from the slope and the intersection of the $\beta_{hkl}\cos(\theta_{hkl})$ vs $4\sin(\theta_{hkl})$ curve with the vertical axis, respectively [36,37]. The dependence of $\beta_{hkl}\cos(\theta_{hkl})$ on $4\sin(\theta_{hkl})$ for the sample is plotted in the inset of Fig. 2(a). Similarly, the crystalline size and microstrain were estimated to be of 507(3) nm and 0.04%, respectively. The high crystalline size and the low value of microstrain verify the high quality of the synthesized sample.

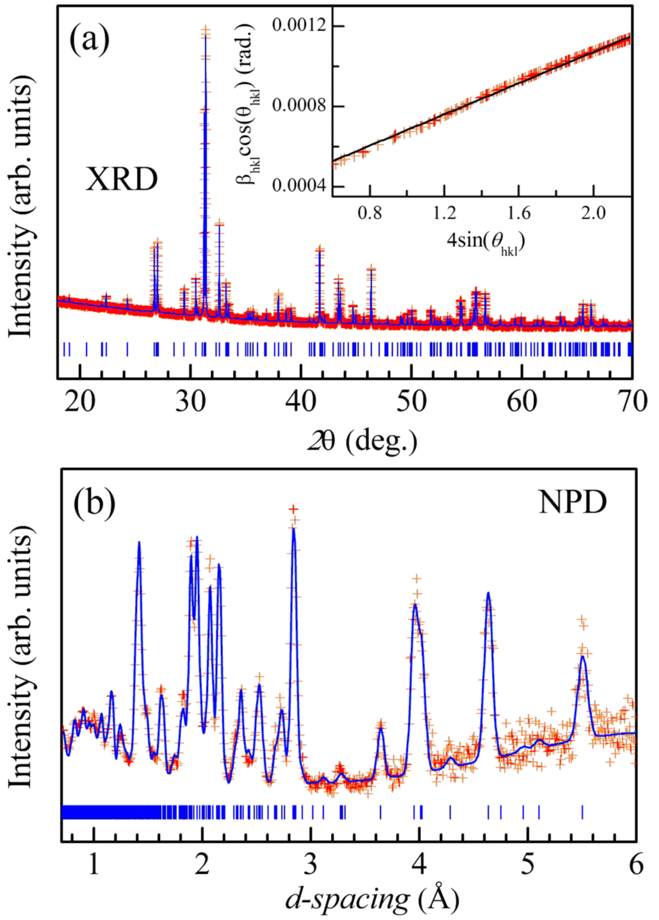

FIG. 2. Room-temperature (a) XRD and (b) NPD patterns of $BaYFeO_4$, refined by the Rietveld method. The experimental points and calculated profiles are shown. The ticks below represent the calculated positions of the nuclear peaks from the structural phase.

The NPD patterns, demonstrating the temperature evolution of the crystal and magnetic structures, are shown in Fig. 3. The data analysis reveals that the initial crystal structure is stable in the entirely studied temperature range. In addition, below 50 K an appearance of magnetic peaks was observed at d_{hkl} around 4.28, 4.98, and 6.42 Å. Below 35 K, one can see a redistribution in magnetic intensity in the d_{hkl} range around 4.28 Å, showing evidence for the modification in the magnetic structure. Both cycloid and SDW magnetic models reported by Thompson *et al.* [27] were attempted to fit the NPD data. It is found that the NPD data with $T \geqslant 35$ K are fitted best to the SDW model. For example, for the 35 K data, the magnetic factor $R_M = 7.44\%$ for the SDW model is much lower than that for the cycloid one (9.66%). On the contrary, at lower temperatures the cycloid model provides the best description of the experimental data. For the 15 K data, $R_M = 7.50\%$ for the SDW and 5.49% for the cycloid model, respectively. Notably, the ordered magnetic moment of about 3.0 μ_B obtained at $T = 15$ K is much smaller than the spin-only one (5.9 μ_B) for the high-spin Fe^{3+} ion ($S = 5/2$),

TABLE I. Refined structural parameters and relevant interatomic distances of $BaYFeO_4$ at room temperature. Space group *Pnma*, $a = 13.1411(2)$ Å, $b = 5.6939(1)$ Å, and $c = 10.2449(2)$ Å.

Atom	Site	X	y	x
Ba1	4*c*	0.209(3)	0.25	0.679(4)
Ba2	4*c*	0.411(3)	0.25	0.397(4)
Y1	4*c*	0.415(3)	0.25	0.017(2)
Y2	4*c*	0.147(2)	0.25	0.313(3)
Fe1	4*c*	0.473(2)	0.25	0.722(3)
Fe2	4*c*	0.190(2)	0.25	0.023(3)
O1	4*c*	0.589(3)	0.25	0.620(4)
O2	4*c*	0.291(3)	0.25	0.178(5)
O3	8*d*	0.006(2)	0.506(5)	0.355(3)
O4	8*d*	0.219(2)	0.510(4)	0.440(3)
O5	8*d*	0.108(4)	−0.002(6)	0.127(4)
	Fe1-O1×1 1.85(5) Å		Fe2-O1×1 1.98(5) Å	
	Fe1-O3×2 1.97(4) Å		Fe2-O2×1 2.07(6) Å	
	Fe1-O5×2 2.02(5) Å		Fe2-O4×2 2.01(3) Å	
			Fe2-O5×2 2.09(5) Å	

indicating a large disordered component of Fe^{3+} moments. These observations are consistent with those of a previous study [27].

B. Magnetic susceptibility

Figure 4 shows the temperature dependence of *dc* magnetization with zero-field-cooled (ZFC) and field-cooled warming (FCW) protocols in the range of 5–400 K under various magnetic fields up to 9 T. In both ZFC and FCW measurements, the data were taken on heating from 5 K. It is clearly seen in Fig. 4 that all $M(T)$ curves exhibit two well-defined peaks at $T_{N1} \sim 50$ K and $T_{N2} \sim 35$ K, corresponding to the SDW and cycloidal AFM orderings of the Fe^{3+} moments. For $\mu_0 H \leqslant 1$ T, FC and ZFC $M(T)$ curves bifurcate below $T^* \sim 17$ K: the FC magnetization increases while the ZFC magnetization decreases sharply with decreasing temperature. The anomaly around T^* (∼17 K) in the *M(T)* curves was also reported in an earlier study [31], and assigned to the occurrence of the spin-glass transition. In case of the present sample, the spin-glass-like transition is also revealed in the temperature dependences of the real part of AC magnetic susceptibility (χ') [Fig. 4(f)] and the remanent magnetization [Fig. 4(g)].

Another particular feature in the $M(T)$ data is an upturn in the magnetization at $T = 200$ K, similar to that reported previously [27,30]. The value of magnetization increases continuously from 200 K to the highest measured temperature (400 K), which implies the absence of a pure paramagnetic phase even above room temperature. Furthermore, along with

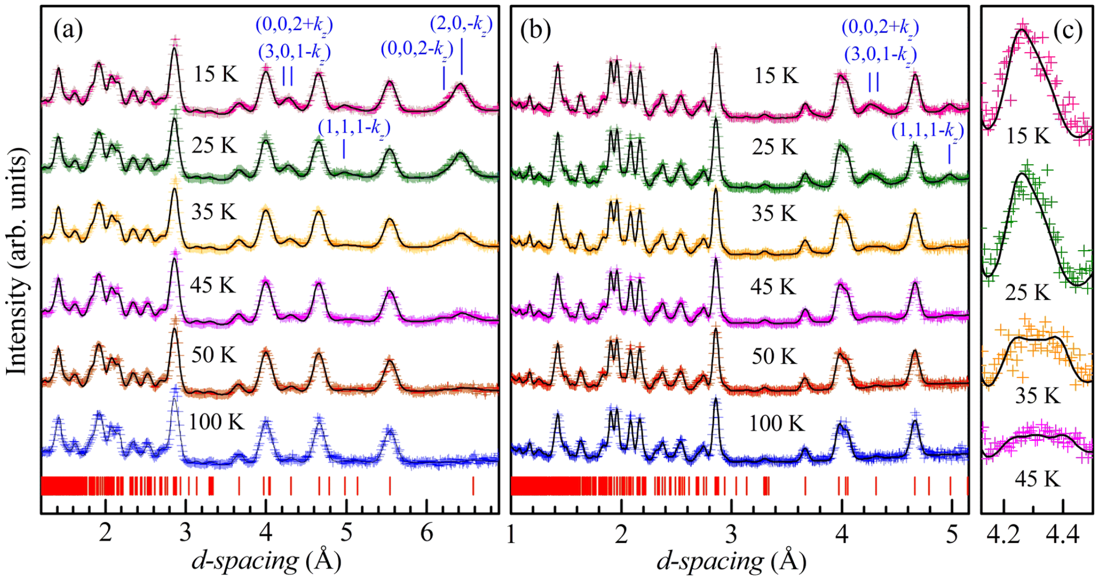

FIG. 3. NPD patterns of $BaYFeO_4$ as a function of temperature collected at scattering angles 2θ of (a) 45.5 ° and (b) 90 ° and processed by the Rietveld method. (c) shows an enlarged section, demonstrating a redistribution in magnetic intensity at the border between the SDW and cycloidal phases. The experimental points and calculated profiles are shown. Vertical ticks below represent calculated positions of the nuclear peaks of the *Pnma* orthorhombic phase. Indices of most intense magnetic peaks are shown.

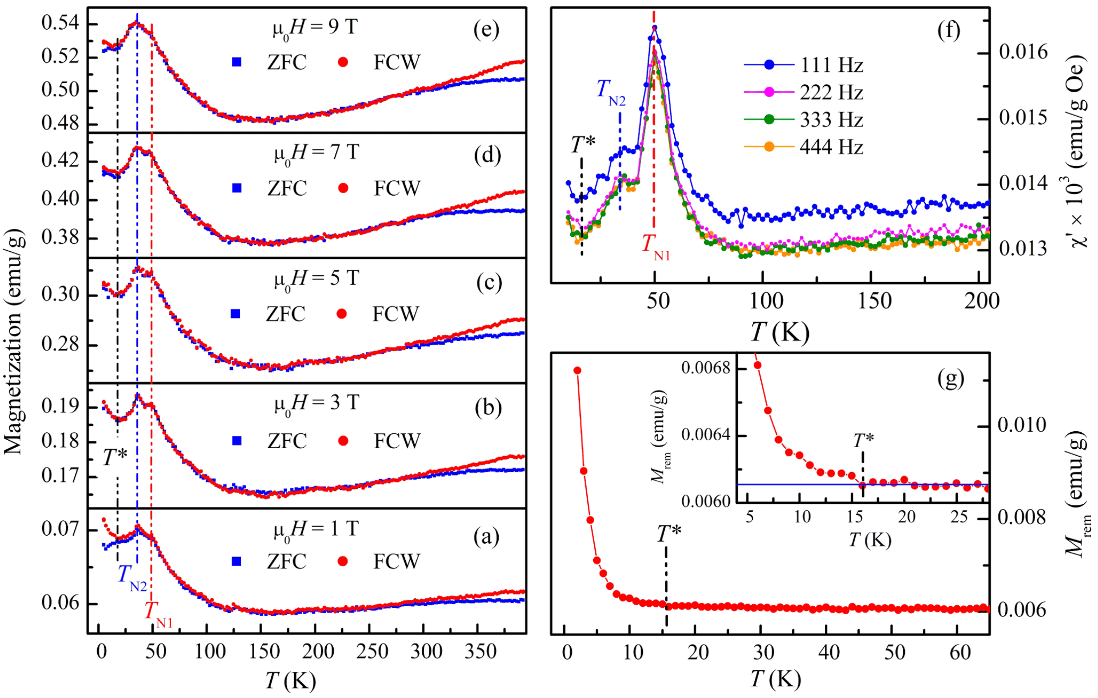

FIG. 4. Temperature-dependent magnetization measured with field-cooled warming (FCW) and zero field-cooled (ZFC) protocols at (a) 1 T, (b) 3 T, (c) 5 T, (d) 7 T, and (e) 9 T. (f) and (g) show the temperature dependences of the real part of AC susceptibility for different frequencies and the remanent magnetization, respectively. The inset in (g) shows a zoomed region around T^* (~17 K). The dashed lines denote the positions at which the magnetic transitions occurred.

the upturn of the magnetization, the separation in ZFC and FCW $M(T)$ curves is also observed above $T = 300$ K . Moreover, a broad maximum at $T \sim 550$ K was observed in the susceptibility vs temperature data by Thompson *et al.* [27], indicating the presence of short-range magnetic correlations at high temperature. Additionally, Cong *et al.* observed a change in resistivity around the magnetic transition at $T = 200$ K, suggesting its intrinsic nature [29]. In contrast, Belik *et al.* [30] suggested that this effect is extrinsic and related it to the presence of magnetic impurities. In the presently studied sample, the absence of any Fe containing magnetic impurity is evident from the diffraction and Mössbauer measurements. Thus, we conclude that the nonparamagnetic behavior is an intrinsic property of $BaYFeO_4$, which is attributed to the presence of short-range magnetic correlations persistent at high temperature.

As can also be seen in Fig. 4, the bifurcation below $T^* \sim 17$ K decreases upon increasing magnetic field and fully disappears in the $M(T)$ curves at $\mu_0H = 3$ T, indicating the suppression of the spin-glass-like state. The peaks associated to the two long-range AFM phases are still visible at $\mu_0H = 9$ T. On the other hand, the isothermal curves obtained at different temperatures of 8–80 K still behave antiferromagnetically with the magnetic fields up to 7 T [Fig. 5(a)]. These findings prove the stabilization of the AFM phases, which contradicts the earlier results reported by Cong *et al.* [29]. In addition, there is a weak magnetic hysteresis loop in all magnetic-field dependent magnetization $M(H)$ curves measured in the temperature range of 10–300 K [Fig. 5(b)], confirming the presence of the short-range magnetic orders that coexist with the dominant AFM ones.

C. Mössbauer spectroscopy

To shed more light on the behavior of the magnetic phases under the application of external magnetic fields, we have performed a systematic Mössbauer study of $BaYFeO_4$ in a wide range of temperatures (4–300 K). At room temperature, the Mössbauer spectrum of $BaYFeO_4$ consists of two doublets D1 and D2 with the close values of isomer shift (*IS*) of 0.37 and 0.30 mm/s but with markedly different quadrupole splittings (*QS*) of 0.23 and 0.50 mm/s, respectively [Fig. 6(a), Table II). These parameters are characteristic of the high spin Fe^{3+} ions in the paramagnetic state. The first doublet D1 with larger $IS = 0.37$ mm/s corresponds to the ferric ions in the octahedral surrounding ($Fe2O_6$) and the second doublet D2 with smaller $IS = 0.30$ mm/s can be attributed to the ferric ions in square pyramids ($Fe1O_5$) in the $BaYFeO_4$ structure. This assignment agrees with the general trend of isomer shifts in oxides: the isomer shift of Fe^{3+} ions decreases with decreasing coordination of iron in FeO_n polyhedra [38]. The higher value of the quadrupole splitting $QS = 0.50$ mm/s for the D2 doublet indicates higher value of the electric field gradient V_{zz} (EFG) for the square pyramid site ($Fe1O_5$) compared to that of the octahedral site ($Fe2O_6$) with $QS = 0.23$ mm/s. Consequently, it indicates that the square pyramids represent less symmetric crystal environment than the octahedra, which is consistent with the structural data of the present and other previous studies [27,28,30,31]. Moreover, in order to check the sample purity, spectra with larger, 12 mm/s velocity sweep were recorded [Fig. 6(b)]. These detailed measurements have revealed that there is no trace of foreign Fe containing phases, in accord with the diffraction data.

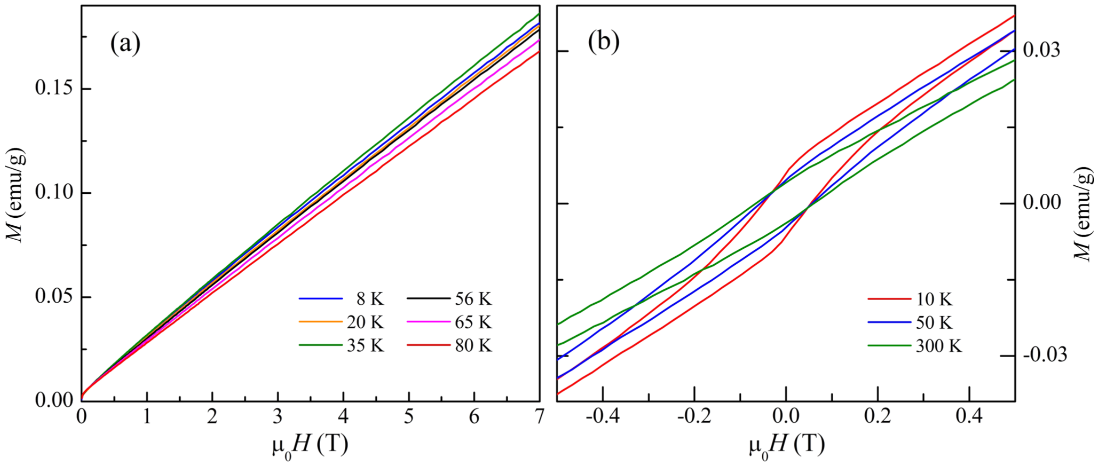

FIG. 5. (a) Magnetic-field dependent isothermal curves and (b) hysteresis loops of $BaYFeO_4$ at selected temperatures.

Furthermore, Mössbauer spectra of $BaYFeO_4$ were collected at low temperatures ranging from 4.2 to 57 K. The paramagnetic doublets remain unchanged until $T_{N1} \sim 50\,K$, below which the spectra are split into magnetic sextets, indicating an onset of the magnetic ordering of iron ions (Fig. 7). The spectra in Figs. 6 and 7 are in good agreement with those previously reported in Ref. [39]. At 4.2 K, the spectral shapes are narrow and well resolved, and they can be decomposed into two well separated sextets corresponding to the two nonequivalent Fe sites. Description using two sextets with distributed values of hyperfine fields H_{hf} is sufficient at 4.2 K, yielding a relatively narrow distribution for the sextet of pyramidal sites and somewhat broader one for the octahedral sites; the remaining Mössbauer parameters were fitted as nondistributed single values. The broad character of the spectral lines and the corresponding H_{hf} distribution are caused by a combination of two effects. The first is the orientation of hyperfine field vector distributed with respect to local structural environment, which leads to a distribution of $QS = \frac{1}{4}eQ \cdot V_{zz} \cdot (3\cos^2\vartheta - 1 + \eta \cdot \sin^2\theta \cdot \cos 2\varphi)$, where η is the asymmetry parameter of the EFG tensor, Q is the quadrupole moment of the ^{57}Fe nuclei, and θ is polar and φ azimuthal angles describing the orientation of H_{hf} with respect to the principal axis system of the EFG. The second is the distribution of hyperfine fields due to its anisotropy. Both effects are naturally caused by the noncollinear structure of Fe magnetic moments, and thus the Mössbauer spectra are compatible with the magnetic structures derived from the neutron diffraction data. In our fitting procedure, the effects of the noncollinear magnetic structure were modeled considering distribution of the H_{hf} magnitudes only, keeping the angles θ and φ as nondistributed parameters. Therefore, the obtained H_{hf} distributions should be viewed as the effective local fields H_{eff}. A broad character of the H_{eff} distribution implies that besides the magnitude the orientation of H_{hf} vectors may be distributed to some extent, as in the case of the spectra described below.

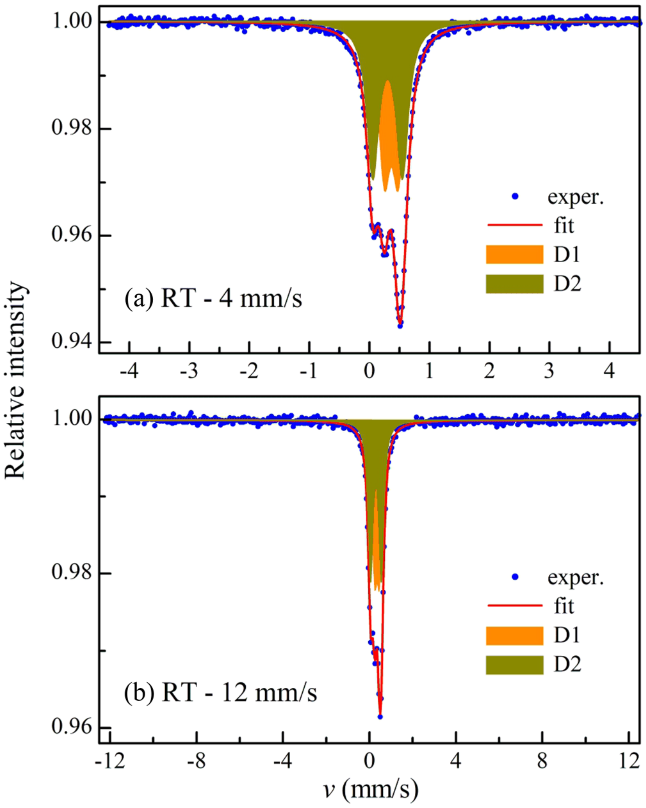

FIG. 6. Room-temperature Mössbauer spectra of $BaYFeO_4$ at different velocity sweeps of 4 mm/s and 12 mm/s. The doublets D1 and D2 correspond to the octahedral and square pyramid sites of Fe^{3+} ions. The spectrum on the top shows the detail of the doublets in a narrow velocity interval, while the bottom spectrum was measured in a wide velocity interval in order to check for sextet(s) that would mean the possible presence of magnetically ordered phase/impurity.

At temperatures about 25 K, the spectral features can be no longer fully described by the two sextets and an additional sextet for the octahedral Fe sites has to be introduced with similar parameters but different values and orientations of hyperfine field with respect to the frame of the EFG tensor. Such a behavior corresponds to distributions of H_{hf} and their orientations similar to those found in Ref. [39]. For consistency, the low temperature spectra (below 27.5 K) were fitted using three sextets with fixed intensity ratio 50:25:25. In the temperature range of 30–50 K, the Mössbauer spectra became even more broadened. This severe broadening is caused by

TABLE II. Parameters obtained from fitting the Mössbauer spectra of $BaYFeO_4$ at selected temperatures. The labels S and D denote sextet and doublet, respectively, IS stands for isomer shift, QS is quadrupole shift/splitting, H_{eff} is the mean effective local magnetic field and σ its standard deviation (where Gaussian distribution of H_{eff} is assumed), or in case of the distributed sextet where it was not possible to resolve components for both crystallographic sites, the broad distribution of effective magnetic field is characterized by its mean (H_{eff} column) and an approximate range (σ column); symbol + denotes mean values of IS and QS parameters. Γ_{exp} is the experimental linewidth (Lorentzian). Parameters denoted by asterisks were fixed in the fitting procedure.

T (K)	Sub-spectrum	Site	IS (mm/s)	QS (mm/s)	$\mu_0 H_{\mathrm{eff}}$ (T)	σ (T)	Γ_{exp} (mm/s)	Intensity (%)
4.2	S_1	Pyramidal	0.41(2)	−0.21(3)	41.0(2)	0.35(5)	0.26(3)	50(2)*
4.2	S_2	Octahedral	0.47(2)	0.06(5)	42.5(4)	0.50(15)	0.26(3)	25(2)*
4.2	S_3	Octahedral	0.47(2)	0.05(3)	43.2(4)	0.50(15)	0.26(3)	25(2)*
25	S_1	Pyramidal	0.42(3)	−0.25(4)	37.4(3)	1.70(9)	0.25(3)	50(2)*
25	S_2	Octahedral	0.47(3)	0.08(4)	37.2(3)	1.08(8)	0.25(3)	25(2)*
25	S_3	Octahedral	0.47(3)	0.09(4)	40.0(3)	1.04(7)	0.25(3)	25(2)*
40	S_{dist}	–	0.43(3)$^+$	−0.13(3)$^+$	20.4(2)	3.5−30.4	0.27(2)*	100
50	D_1	Pyramidal	0.40(2)	0.50(3)	–	–	0.26(3)	50(1)
50	D_2	Octahedral	0.48(2)	0.23(3)	–	–	0.26(3)	50(1)
296	D_1	Pyramidal	0.30(2)	0.50(2)	–	–	0.24(2)	53(1)
296	D_2	Octahedral	0.35(2)	0.21(2)	–	–	0.24(2)	47(1)

the fact that in the SDW phase, not only directions of Fe magnetic moments are changing but also their magnitudes, and both types of change are then valid also for the hyperfine magnetic fields [39–45]. These variations exceed the differences of QS between the two Fe crystallographic sites, and as a consequence, the experimental spectra were fitted by a single sextet component with a very wide distribution of H_{eff} and average value of IS. Mössbauer parameters for all selected temperatures are collected in Table II.

Temperature dependences of quadrupole shifts/splitting, effective local magnetic fields, and isomer shifts, displayed in Fig. 8, were obtained using the fitting procedure described above. The parameters demonstrate anomalous changes at the border $T = 30\,\mathrm{K}$ between the SDW and cycloid phases, where the description by three sextets had to be replaced by a sextet with a wide distribution of H_{eff}. Also, up to 27 K, the absolute values of QS grew with increasing temperature, which could be connected with ongoing changes in electric polarization. Slight continuous changes of magnetic structure could, however, also influence QS, as the splitting is affected also by the spatial orientation of magnetic moments. Furthermore, the magnetic hyperfine field H_{hf} is antiparallel and proportional to the iron magnetic moment μ_{Fe} via the relation $H_{\mathrm{hf}}(T) \approx 11\mu_{\mathrm{Fe}}(\mu_{\mathrm{B}})$ [39,41,46]. Therefore, it can be derived from the obtained temperature-dependent curve of H_{eff}, that the magnetic moment μ_{Fe} of the cycloidal order continuously increases with decreasing temperature without any decrease through the spin-glass transition, which is not typical for certain reentrant systems [47,48]. This indicates that the spin-glass-like phase is not formed on the same magnetic sublattice of the long-range cycloidal order. In previous studies on $BaYFeO_4$, it was also evidenced that due to a high degree of magnetic frustration some amount of Fe^{3+} spins remained paramagnetically disordered well below the T_{N1} and T_{N2} temperatures and froze out only below T^* in the form of the spin-glass state [27,31].

For a pure paramagnetic phase, the application of external magnetic field H should lead to magnetic sextets with effective magnetic field H_{eff} roughly equal to the applied field. In our case, the Mössbauer spectrum at $T = 57\,\mathrm{K}$ and $\mu_0 H = 6\,\mathrm{T}$ (Fig. 9) is composed of two very broad magnetic sextets with the actual fields different from the value of applied field, reflecting the presence of a small internal magnetic hyperfine field. Without applied field, the AFM short-ranged ordered spins act as paramagnetic ones and their rapid reorientations lead to zero time-averaged hyperfine fields. As the applied field slightly polarizes the paramagnetic ensemble, some small magnetization is induced, and this leads to nonzero effective fields.

Compared to the applied field strength, the H_{eff} of high-spin Fe^{3+} in the octahedral site increased by 2.2 T, whereas the H_{eff} of high-spin Fe^{3+} in the squared pyramid site decreased by 1.2 T. Although the alignment of magnetic moments between the octahedral and squared pyramidal sites is indicated to be antiparallel, such inequality of induced hyperfine fields indicates the existence of two sublattices with two different exchange interactions. This behavior can be attributed to the presence of short-range AFM correlations, probably between nearest neighbor spins in columns of edge-sharing rings Fe_4O_{18} [Fig. 1(b)], and weaker interactions with more distant Fe neighbors.

For $T = 27.5\,\mathrm{K}$, which is in the range of the cycloidal magnetic structure, the application of a magnetic field up to 6 T caused only a broadening of the magnetic sextets. The evaluated distribution of effective H_{eff} did not change its position, only became broadened, hence the character of the spectra [Figs. 10(a) and 10(b)] implies the stable AFM order. The spectrum at 40 K, where the SDW magnetic structure is assumed, is significantly broadened already without application of external field, due to the effects connected with magnitude of Fe moments in the SDW phase. Therefore, it is difficult to evaluate the influence of external magnetic field. In contrast, below $T^* \sim 17\,\mathrm{K}$, where the cycloidal AFM and the spin-glass states presumably coexist, the Mössbauer spectra were strongly affected by the external magnetic fields.

Figure 11 shows the evolution of Mössbauer spectra at 4.2 K as a function of the applied magnetic field H. As

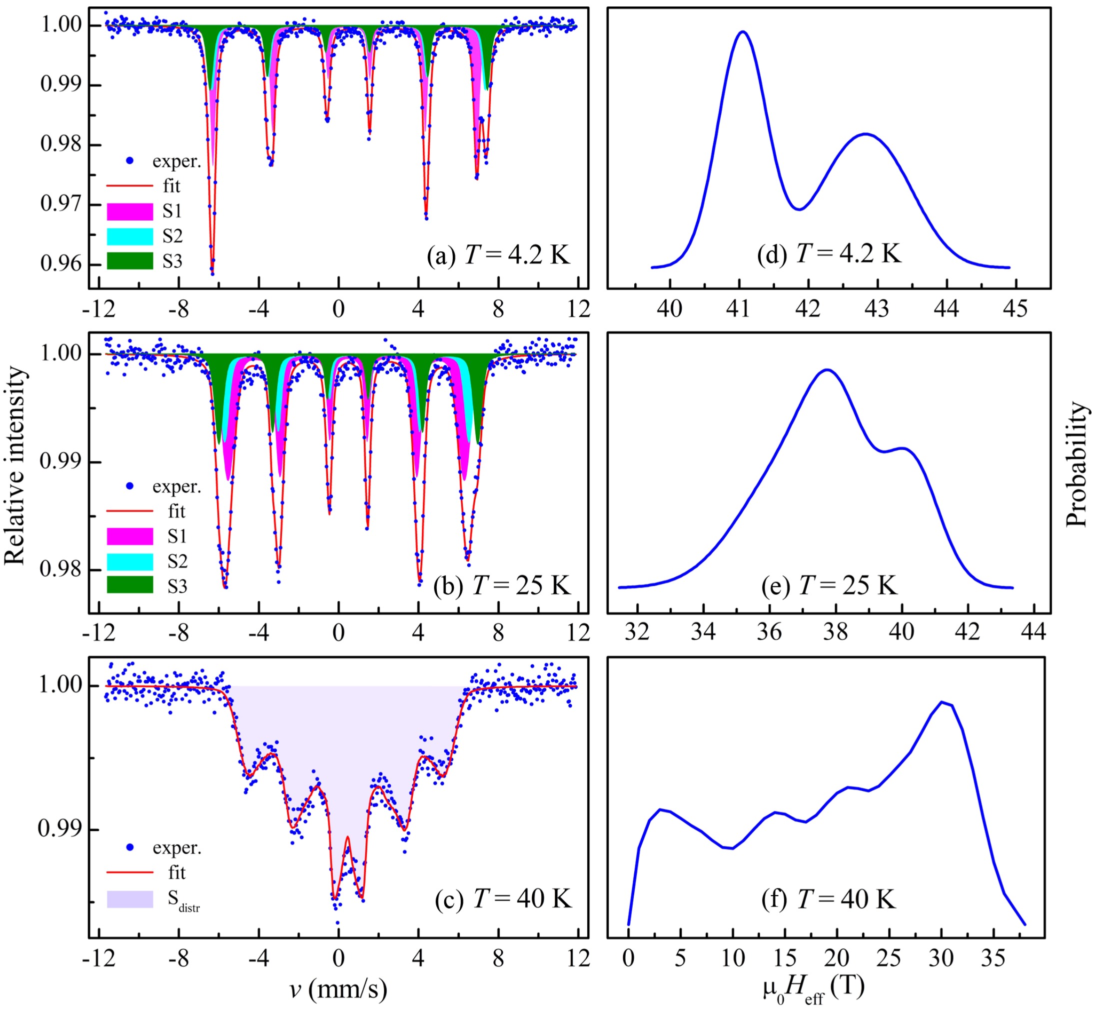

FIG. 7. Selected Mössbauer spectra of $BaYFeO_4$ at low temperatures (left) and the corresponding distributions of effective hyperfine magnetic field (right) as evaluated from the fits.

mentioned above, the description using two sextets with intensity ratio 3:2:1:1:2:3 (corresponding to the powder sample with random orientation of particles with respect to direction of γ rays) is sufficient in order to capture all features of the experimental spectrum at this temperature and zero magnetic field, and the magnetic sextets become only broadened for $\mu_0 H = 2\,\mathrm{T}$, similarly to the behavior observed in the higher temperature range. On the other hand, for $\mu_0 H > 2\,\mathrm{T}$ there is a notable change in the relative intensity of the second and fifth peaks with respect to the remaining peaks, and therefore an additional pair of sextets had to be used in the fitting procedure. For each of the two Fe sites, two sextets were used with ratio of line intensities 3:b:1:1:b:3, where $b = 4\sin^2 q/(1 + cos^2 q)$, θ is the angle between the direction of γ rays and H_{hf} (H_{eff}). These ratios were different from the 3:2:1:1:2:3 intensity ratio observed for the zero-field antiferromagnetic sextets (Fig. 11). Our fits yielded one type of sextets (S1, S2) with $b < 2$ and the other type (S1a, S2a) with $b > 2$. In our experimental setup, where the external magnetic field is applied perpendicularly to the direction of γ rays, both types of sextets correspond to magnetic moments being affected by the applied magnetic field: the limiting cases of intensity ratios would be 3:0:1:1:0:3 for hyperfine field completely parallel to the γ rays (i.e., perpendicular to the external field) and 3:4:1:1:4:3 for hyperfine field completely perpendicular to the γ rays, i.e., (anti)parallel to the external field [49]. In both cases, the Fe moments of octahedral and pyramid Fe are mutually oriented antiparallel, but for $b < 2$ their moments are rotated towards the direction of the γ rays, i.e., perpendicular to the external magnetic field. Such a component can be considered as the original phase, unperturbed by the field. The latter case with $b > 2$ corresponds to the situation where the antiferromagnetically coupled pair of neighboring Fe moments is, to some extent, aligned with the external field, and can be considered as the component affected (rotated) by the magnetic field. Naturally, a stronger external field should orient larger portions of Fe moments towards its direction, hence the content of the latter type of sextets increases with increasing field; the intensity of S1a+S2a at 2 T is too low for a stable fit (its estimate is well below 20%), while for 4 T the intensity of S1a+S2a is about 38(2)%, and about 66(2)% for 6 T. Although the correspondence of the two types of Mössbauer sextets with microscopic scenarios is only approximate, the fraction of structure perturbed by the field will depend in a similar manner on the external magnetic field.

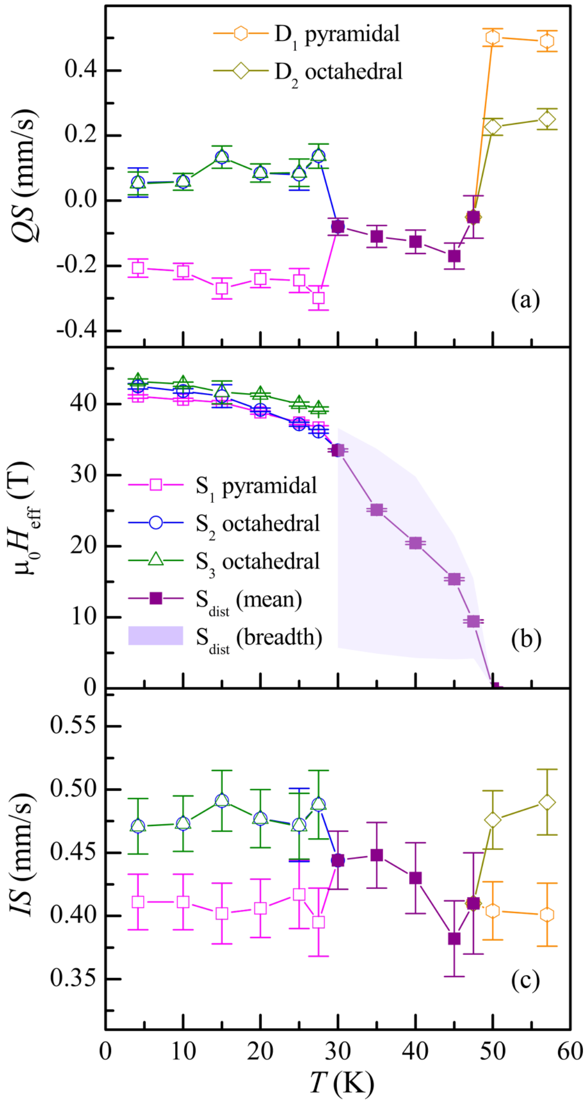

FIG. 8. Temperature dependences of quadrupole shift (quadrupole splitting above 50 K), effective local magnetic field, and isomer shift.

Furthermore, in the highest fields the neighboring Fe pairs are not oriented randomly by the field, as indicated by the increase of H_{eff} for the octahedral sextet S2a and the decrease of H_{eff} for the pyramidal sextet. This agrees with behavior at $T = 57\,\mathrm{K}$ and $\mu_0 H = 6\,\mathrm{T}$ where a similar inequality of H_{eff} was observed. The cause for such polarization must lie in uneven magnitudes of the Fe moments in the pyramidal and octahedral sites. Because the hyperfine field at the Fe nuclei is oriented antiparallel to the direction of the atomic magnetic moment, the moment of octahedral Fe must be aligned antiparallel to the applied field (and is thus smaller than the moment of Fe in the pyramidal sites) while the moment of pyramidal Fe is parallel to the field. The observed behavior of MS under applied fields lies in with the findings from magnetic measurements where the cycloidal AFM phase was revealed to be stable under magnetic fields up to 6 T, and the high-field ferromagnetic phase was raised from the zero-field spin glass. The strong sensitivity of the spin-glass phase regions to the moderate applied magnetic fields implies their more pronounced magnetic frustration degree in comparison with the cycloid regions, coexisting below T^*. A possible reason for this effect may be a presence of oxygen defects at the grain boundaries in the polycrystalline $\mathrm{BaYFeO_4}$ sample within the spin-glass regions, weakening Fe-O-O-Fe interchain interactions between the neighboring folded-ladder chain units formed by the $\mathrm{Fe_4O_{18}}$ tetramer units, resulting in uncorrelated magnetic behavior of such units in the vicinity of the defects in the absence of applied magnetic fields.

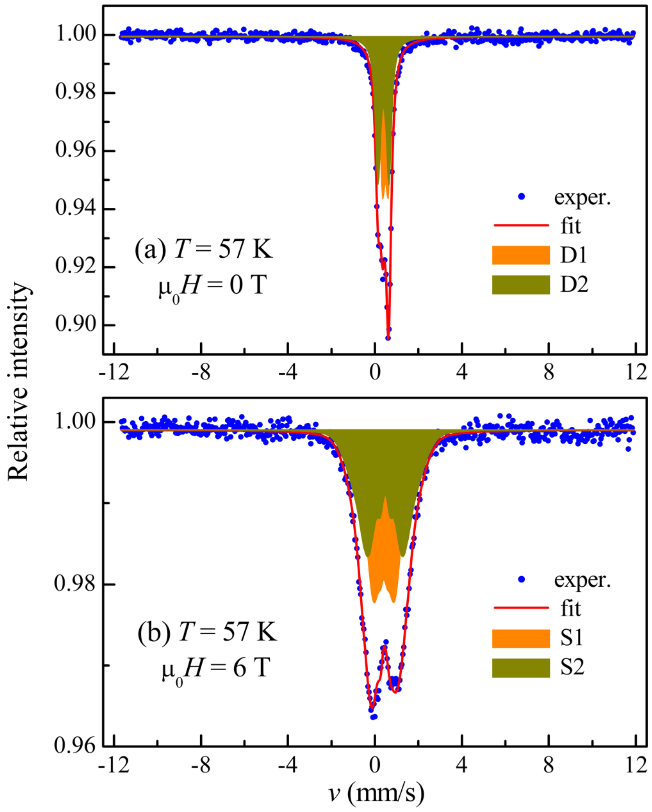

FIG. 9. Mössbauer spectra of $\mathrm{BaYFeO_4}$ at 57 K under (a) zero and (b) 6 T applied external magnetic field.

D. Magnetocaloric effect

In order to access the nature of the different magnetic transitions in $\mathrm{BaYFeO_4}$ and probe the magnetic field dependence of these transitions, the magnetocaloric effect is exploited as a fundamental research probe [50–53]. On subjecting the magnetic sample to a change of external magnetic field at a constant temperature, the isothermal entropy change, ΔS_{M}, can be calculated with the help of the following Maxwell relation [54]:

$$\left(\frac{\partial S_M(T,H)}{\partial H}\right)_T = \mu_0\left(\frac{\partial M(T,H)}{\partial T}\right)_H, \tag{1}$$

from which the numerical value of ΔS_{M} is given by the following equation:

$$\Delta S_M(T,H) = \mu_0 \int_0^H \left(\frac{\partial M}{\partial T}\right)_H dH \tag{2}$$

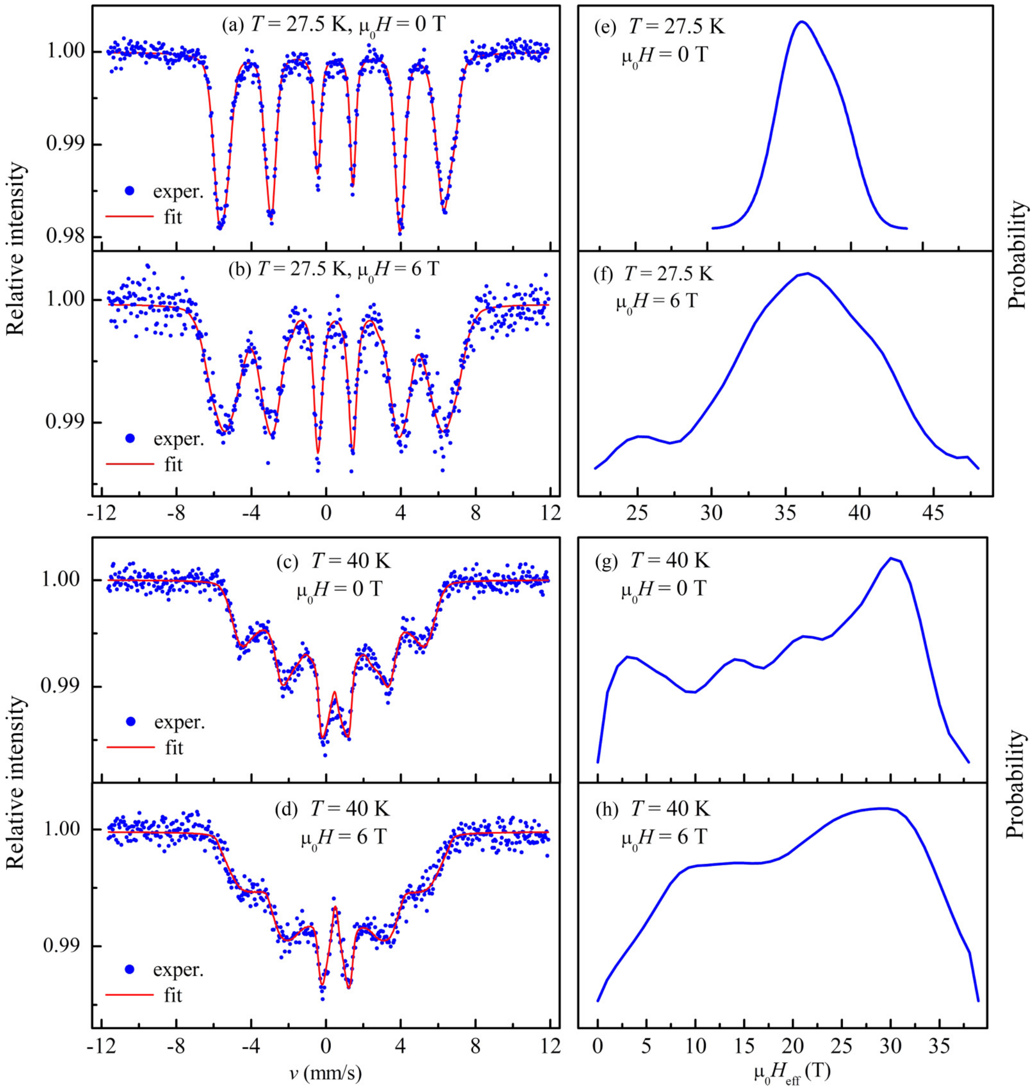

FIG. 10. Mössbauer spectra of $BaYFeO_4$ under zero and 6 T applied external magnetic field at $T = 40$ K and 27.5 K (left) and the corresponding distributions of effective magnetic fields H_{eff} H_{eff} (right).

With the help of the isothermal curves obtained for the temperature range of 8–80 K (Fig. 5), the magnetic entropy change is calculated for $\mu_0\Delta H = 0\text{–}7$ T and shown in Fig. 12. It is worth noting that ΔS_{M} (T) is provided by the slope of M vs T curves obtained at different fields, making it more sensitive for probing magnetic phase transitions compared to conventional magnetization data. Generally, ΔS_{M} (T) is positive for an AFM ordering due to magnetic-field-induced spin disorder in magnetic sublattices antiparallel to the applied magnetic field, increasing the magnetic entropy [51,55]. On the other hand, a FM transition results in a negative value of ΔS_{M} because of more magnetically ordered configuration with the magnetic field, decreasing the magnetic entropy [51,55].

As can be seen in Fig. 12(a), for the small magnetic field range (0.02–0.36 T), the ΔS_{M} (T) curves illustrate three positive peaks at $T = 55$, 32 and 17 K, corresponding to the magnetic phase transitions to the SDW AFM, cycloidal AFM, and spin-glass states. With increasing the magnetic field, the positive sign of the peak at T_{N2} (∼32 K) remains unchanged up to the highest magnetic field of 7 T, indicating the robustness of the cycloidal AFM phase. A contrary behavior was observed for the ΔS_{M} (T) peaks at T^* (∼17 K) and T_{N1} (∼50 K). Both the ΔS_{M} peaks first increase in magnitude with increasing H up to a critical magnetic field named as H_1 and then decrease and reach zero at the second critical magnetic field named as H_2. Above H_2, they are negative and become more negative with further increasing H up to 7 T. The values of H_1 and H_2 are $\mu_0 H_1 = 0.16$ T and $\mu_0 H_2 = 0.33$ T for the peak at T_{N1}, which are much smaller than $\mu_0 H_1 = 1$ and $\mu_0 H_2 = 1.9$ T for the peak at T^* (∼17 K) (Fig. 12). As can be seen in Fig. 12, the peak at T^* (∼17 K) disappeared when the applied magnetic field exceeded 2 T. Moreover, we observed the emergence of the negative peak around 11 K in the $\Delta S_{\text{M}}(\text{T})$ curves at $\mu_0 H \geqslant 2$ T [Fig. 12(c)], which is consistent with the observation from the magnetic field dependence of the ΔS_{M} $(\mu_0 H)$ at different temperatures (Fig. 13) that ΔS_{M} at 11 K became larger in magnitude compared to those at 8 K and 14 K at $\mu_0 H > 1$ T [see the inset of Fig. 13(d)]. The phenomenon can be attributed to the magnetic-field-induced

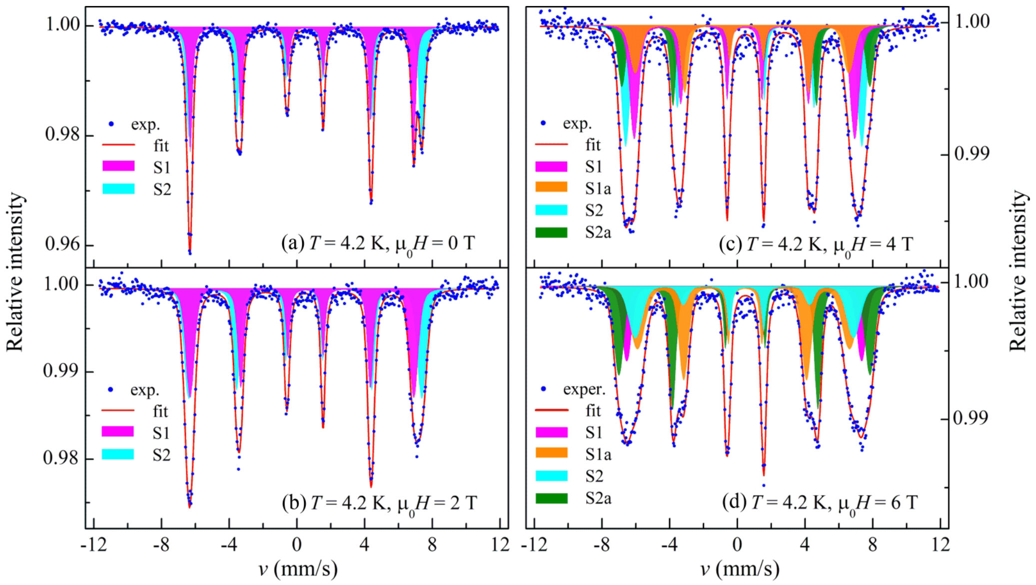

FIG. 11. External magnetic field dependence of Mössbauer spectra of $BaYFeO_4$ at 4.2 K. S1 and S1a correspond to zero-field and high-field sextets belonging to the pyramidal sites. S2 and S2a denote zero-field and high-field octahedral magnetic sextets of the octahedral sites.

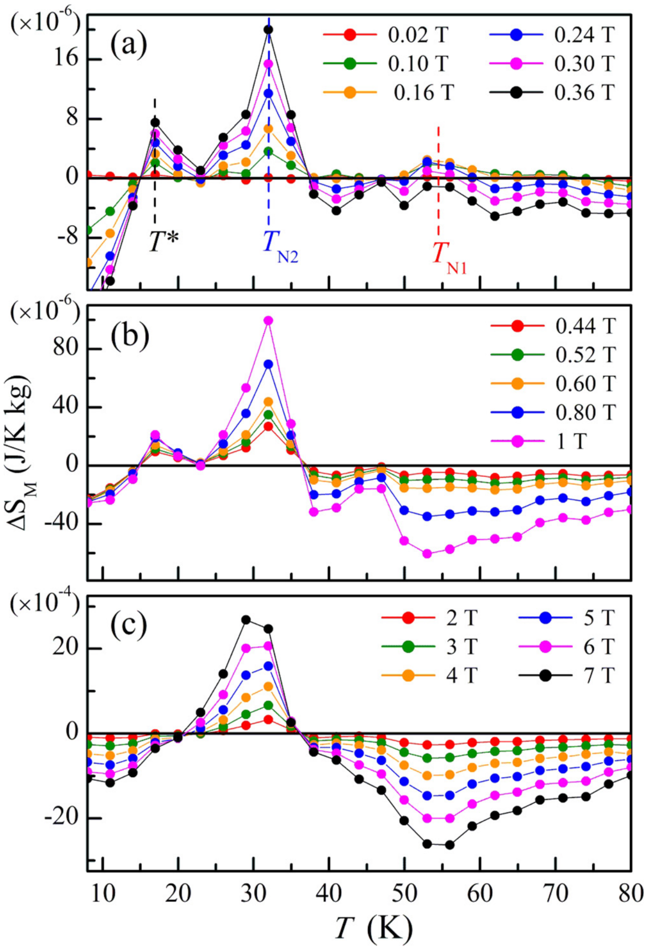

FIG. 12. Temperature dependence of magnetic entropy change ΔS_M at different fields of (a) 0.02–0.36 T, (b) 0.44–1 T, and (c) 2–7 T.

spin-glass – FM crossover, consistent with the Mössbauer results.

The details of the local features in the entropy change are best understood through an examination of its field dependence at several representative temperatures, as shown in Fig. 13. For temperatures above T_{N1} [Fig. 13(a)], the positive sign of ΔS_M and its increase with increasing magnetic field strength at low H are signatures of short-range AFM ordering. As the applied magnetic field is strong enough to align spins of the short-range AFM entities, ΔS_M decreases with increasing H. The observation is consistent with the magnetic-field-induced PM to ferrimagnetic phase transition found by the Mössbauer study. Furthermore, it can be seen in Fig. 13(b) that for the SDW phase temperature range of 38–53 K, ΔS_M shows a behavior similar to that observed for the paramagnetic range. It indicates the coexistence of the short-range and SDW phases and the contribution to ΔS_M from the short-range phase is dominant over that from the SDW one. As the temperature is lowered, the decrease in magnitude of the negative ΔS_M is attributed to the expansion of the SDW phase at the expense of the short-range phase.

In the temperature range of 20–35 K [Fig. 13(c)], the positive sign of ΔS_M and its monotonous increase with increasing applied field up to 7 T are typical for an AFM material, indicating the stabilization of the cycloidal AFM phase as also confirmed by the Mössbauer study. At temperatures around the spin-glass transition [Fig. 13(d)], ΔS_M is characterized by the emergence of a positive peak at the critical magnetic field $\mu_0H_1 \sim 1$ T, above which it monotonously decreases as the magnetic field increases. As the temperature is lowered below 14 K, the spin-glass phase develops and its contribution to ΔS_M becomes dominant [Fig. 13(c)], resulting in the negative sign of ΔS_M in all the magnetic field ranges. It is worth noticing from the inset of Fig. 13(d) that ΔS_M exhibits a rapid

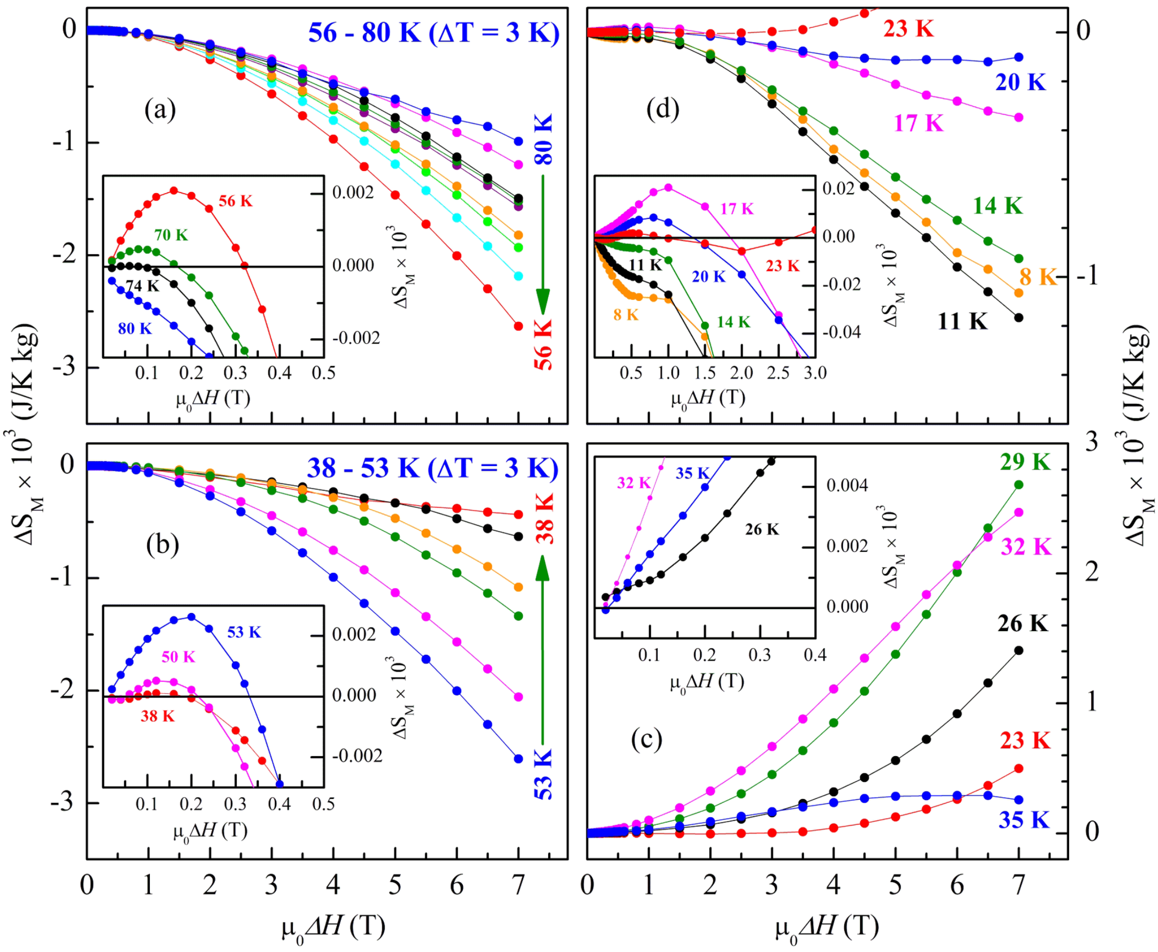

FIG. 13. Magnetic field dependence of magnetic entropy change ΔS_M at temperature ranges of (a) 56–80 K, (b) 38–53 K, (c) 23–35 K, and (d) 8–20 K.

increase in slope at $\mu_0 H_1 \sim 1$ T, which could be considered as a critical magnetic field at which the spin-glass phase started to be converted into the FM phase, which is also revealed by the Mössbauer results. Notably, the critical field H_1 corresponds to a sharp decrease of the ferroelectric polarization by two times as reported by Cong *et al.* [29]. In this context, our observations pinpoint that the magnetic field-induced modification of the spin correlations from the AFM to FM character in the spin-glass state, which also may persist above T^*, is a possible reason for the magnetic field dependence of ferroelectricity in $BaYFeO_4$. The observation of the correlated behaviors of the spin-glass state and ferroelectricity in high magnetic fields could be explained by the presence of regions with FM correlations, suppressing the spontaneous ferroelectric polarization formed in the surrounding cycloidal AFM regions via magnetic proximity effects. Further theoretical and experimental investigations are needed to elucidate this mechanism and its impact on the magnetoelectric coupling in the system.

IV. CONCLUSION

The temperature and magnetic field effects on the magnetic properties of $BaYFeO_4$ have been investigated systematically. The complex magnetic nature is uncovered, resulting from the geometrical magnetic frustration. The long-range SDW AFM ordering of Fe^{3+} spins occurs at $T_{N1} \sim 50$ K, which then transforms into the cycloidal AFM state at $T_{N2} \sim 35$ K. Below $T^* \sim 17$ K, the system enters the spin-glass-like state, which coexists with the long-range cycloidal one. Under the application of external magnetic fields, the long-range SDW and cycloidal AFM states are robust up to 6 T. In contrast, the spin-glass state is strongly affected by the applied magnetic field, and the character of spin correlations is modified from the AFM to FM one. The correlated behavior of this effect with the previously observed suppression of ferroelectric polarization underlines a crucial role of the spin-glass state in the magnetoelectric effect in $BaYFeO_4$.

ACKNOWLEDGMENTS

The work was supported by the RFBR and VAST Grant No. 20-52-54002. Vietnamese researchers were supported by the Vietnam Academy of Science and Technology under the Program of development in the field of physics by 2020, Grant No. VAST.CTVL.01/17-20 and the RFBR–VAST cooperation program, Grant No. QTRU01.02/20-21. L.T.P.T. was funded by Vingroup Joint Stock Company and supported by the Domestic Master/PhD Scholarship Programme of Vingroup Innovation Foundation

(VINIF), Vingroup Big Data Institute (VINBIGDATA), code VINIF.2020.TS.85. In South Korea, the work was supported by National Research Foundation of Korea (NRF) grants funded by the Korea government's Ministry of Science and ICT (MSIT, No. NRF-2017R1A2B4010490 and No. 2020R1A2B5B01002184). Work at USF (magnetic and MCE studies) was supported by the U.S. Department of Energy, Office of Basic Energy Sciences, Division of Materials Sciences and Engineering under Award No. DE-FG02-07ER46438. We thank Dr. Veverka for measurements of temperature dependence of remanence, performed in MGML-Materials Growth & Measurement Laboratory [56], which is supported within the program of Czech Research Infrastructures (Project No. LM2018096).

[1] M. Kenzelmann, A. B. Harris, S. Jonas, C. Broholm, J. Schefer, S. B. Kim, C. L. Zhang, S.-W. Cheong, O. P. Vajk, and J. W. Lynn, Phys. Rev. Lett. **95**, 087206 (2005).
[2] J. Van Den Brink and D. I. Khomskii, J. Phys.: Condens. Matter **20**, 434217 (2008).
[3] S.-W. Cheong and M. Mostovoy, Nat. Mater. **6**, 13 (2007).
[4] T. Kimura, T. Goto, H. Shintani, K. Ishizaka, T. Arima, and Y. Tokura, Nature (London) **426**, 55 (2003).
[5] W. Eerenstein, N. D. Mathur, and J. F. Scott, Nature (London) **442**, 759 (2006).
[6] T. Lottermoser, T. Lonkai, U. Amann, D. Hohlwein, J. Ihringer, and M. Fiebig, Nature (London) **430**, 541 (2004).
[7] H. W. Brinks, J. Rodríguez-Carvajal, H. Fjellvåg, A. Kjekshus, and B. C. Hauback, Phys. Rev. B **63**, 094411 (2001).
[8] F. Ye, B. Lorenz, Q. Huang, Y. Q. Wang, Y. Y. Sun, C. W. Chu, J. A. Fernandez-Baca, P. Dai, and H. A. Mook, Phys. Rev. B **76**, 060402(R) (2007).
[9] I. V. Solovyev, Phys. Rev. B **87**, 144403 (2013).
[10] Y. Yamasaki, S. Miyasaka, Y. Kaneko, J. P. He, T. Arima, and Y. Tokura, Phys. Rev. Lett. **96**, 207204 (2006).
[11] V. Y. Pomjakushin, M. Kenzelmann, A. Dönni, A. B. Harris, T. Nakajima, S. Mitsuda, M. Tachibana, L. Keller, J. Mesot, H. Kitazawa, and E. Takayama-Muromachi, New J. Phys. **11**, 043019 (2009).
[12] Y. J. Choi, H. T. Yi, S. Lee, Q. Huang, V. Kiryukhin, and S. W. Cheong, Phys. Rev. Lett. **100**, 047601 (2008).
[13] H. Kimura, Y. Noda, and K. Kohn, J. Magn. Magn. Mater. **321**, 854 (2009).
[14] S. Ishihara, J. Phys. Soc. Jpn. **79**, 011010 (2010).
[15] H. Katsura, N. Nagaosa, and A. V. Balatsky, Phys. Rev. Lett. **95**, 057205 (2005).
[16] I. A. Sergienko and E. Dagotto, Phys. Rev. B **73**, 094434 (2006).
[17] C. R. dela Cruz, B. Lorenz, Y. Y. Sun, Y. Wang, S. Park, S.-W. Cheong, M. M. Gospodinov, and C. W. Chu, Phys. Rev. B **76**, 174106 (2007).
[18] Y. Yamaguchi, T. Nakano, Y. Nozue, and T. Kimura, Phys. Rev. Lett. **108**, 057203 (2012).
[19] K. Dey, A. Indra, D. De, S. Majumdar, and S. Giri, ACS Appl. Mater. Interfaces **8**, 12901 (2016).
[20] S. Sharma, T. Basu, A. Shahee, K. Singh, N. P. Lalla, and E. V. Sampathkumaran, Phys. Rev. B **90**, 144426 (2014).
[21] N. Reynolds, A. Mannig, H. Luetkens, C. Baines, T. Goko, R. Scheuermann, L. Keller, M. Bartkowiak, A. Fujimura, Y. Yasui, C. Niedermayer, and J. S. White, Phys. Rev. B **99**, 214443 (2019).
[22] D. D. Khalyavin, P. Manuel, and L. C. Chapon, Phys. Rev. B **85**, 220401(R) (2012).
[23] F. Cinti, A. Cuccoli, and A. Rettori, Phys. Rev. B **83**, 174415 (2011).
[24] H. Kawamura, J. Phys.: Condens. Matter **23**, 164210 (2011).
[25] Y. Yamaguchi and T. Kimura, Nat. Commun. **4**, 2063 (2013).
[26] E. E. Gordon, S. Derakhshan, C. M. Thompson, and M. H. Whangbo, Inorg. Chem. **57**, 9782 (2018).
[27] C. M. Thompson, J. E. Greedan, V. O. Garlea, R. Flacau, M. Tan, P. T. Nguyen, F. Wrobel, and S. Derakhshan, Inorg. Chem. **53**, 1122 (2014).
[28] F. Wrobel, M. C. Kemei, and S. Derakhshan, Inorg. Chem. **52**, 2671 (2013).
[29] J.-Z. Cong, S.-P. Shen, Y.-S. Chai, L.-Q. Yan, D.-S. Shang, S.-G. Wang, and Y. Sun, J. Appl. Phys. **117**, 174102 (2015).
[30] A. A. Belik, N. Terada, Y. Katsuya, M. Tanaka, I. S. Glazkova, A. V. Sobolev, I. A. Presniakov, and K. Yamaura, J. Alloys Compd. **811**, 151963 (2019).
[31] S. Ghara and A. Sundaresan, J. Phys.: Condens. Matter **30**, 245802 (2018).
[32] V. L. Aksenov, A. M. Balagurov, V. P. Glazkov, D. P. Kozlenko, I. V. Naumov, B. N. Savenko, D. V. Sheptyakov, V. A. Somenkov, A. P. Bulkin, V. A. Kudryashev, and V. A. Trounov, Physica B **265**, 258 (1999).
[33] J. Rodríguez-Carvajal, Physica B **192**, 55 (1993).
[34] T. Žák and Y. Jirásková, Surf. Interface Anal. **38**, 710 (2006).
[35] Z. Klencsár, E. Kuzmann, and A. Vértes, J. Radioanal. Nucl. Chem. **210**, 105 (1996).
[36] V. Biju, N. Sugathan, V. Vrinda, and S. L. Salini, J. Mater. Sci. **43**, 1175 (2008).
[37] E. J. Mittemeijer and U. Welzel, Z. Krist. **223**, 552 (2008).
[38] F. Menil, J. Phys. Chem. Solids **46**, 763 (1985).
[39] I. S. Glazkova, A. A. Belik, A. V. Sobolev, M. N. Smirnova, N. S. Ovanesyan, and I. A. Presniakov, J. Phys. Chem. C **124**, 13374 (2020).
[40] A. V. Sobolev, A. A. Akulenko, I. S. Glazkova, D. A. Pankratov, and I. A. Presniakov, Phys. Rev. B **97**, 104415 (2018).
[41] D. Colson, A. Forget, and P. Bonville, J. Magn. Magn. Mater. **378**, 529 (2015).
[42] A. Sobolev, V. Rusakov, A. Moskvin, A. Gapochka, A. Belik, I. Glazkova, A. Akulenko, G. Demazeau, and I. Presniakov, J. Phys.: Condens. Matter **29**, 275803 (2017).
[43] M. Duttine, A. Wattiaux, F. Balima, C. Decorse, H. Moutaabbid, D. H. Ryan, and P. Bonville, AIP Adv. **9**, 035008 (2019).
[44] I. Presniakov, V. Rusakov, A. Sobolev, A. Gapochka, M. Matsnev, and A. A. Belik, Hyperfine Interact. **226**, 41 (2014).
[45] A. Palewicz, T. Szumiata, R. Przeniosło, I. Sosnowska, and I. Margiolaki, Solid State Commun. **140**, 359 (2006).
[46] J. Chappert, J. Phys. Colloq. **35**, C6-71 (1974).
[47] S. Chillal, M. Thede, F. J. Litterst, S. N. Gvasaliya, T. A. Shaplygina, S. G. Lushnikov, and A. Zheludev, Phys. Rev. B **87**, 220403(R) (2013).

[48] A. Kumar, S. D. Kaushik, V. Siruguri, and D. Pandey, Phys. Rev. B **97**, 104402 (2018).

[49] A. G. Maddock, *Mössbauer Spectroscopy: Principles and Applications of the Techniques* (Horwood Publishing, Ltd., Albio, UK, 1998).

[50] P. Lampen, N. S. Bingham, M. H. Phan, H. Srikanth, H. T. Yi, and S. W. Cheong, Phys. Rev. B **89**, 144414 (2014).

[51] N. S. Bingham, P. Lampen, M. H. Phan, T. D. Hoang, H. D. Chinh, C. L. Zhang, S. W. Cheong, and H. Srikanth, Phys. Rev. B **86**, 064420 (2012).

[52] R. P. Madhogaria, R. Das, E. M. Clements, V. Kalappattil, M. H. Phan, H. Srikanth, N. T. Dang, D. P. Kozlenko, and N. S. Bingham, Phys. Rev. B **99**, 104436 (2019).

[53] E. M. Clements, R. Das, L. Li, P. J. Lampen-Kelley, M. H. Phan, V. Keppens, D. Mandrus, and H. Srikanth, Sci. Rep. **7**, 6545 (2017).

[54] M. H. Phan and S. C. Yu, J. Magn. Magn. Mater. **308**, 325 (2007).

[55] M. H. Phan, M. B. Morales, N. S. Bingham, H. Srikanth, C. L. Zhang, and S. W. Cheong, Phys. Rev. B **81**, 094413 (2010).

[56] Measurements of temperature dependence of remanence were performed in MGML-Materials Growth & Measurement Laboratory (http://www.mgml.eu).

Correction: The surname of the 12th author contained an error and has been fixed.